

pubs.acs.org/cm Article

Enabling Ambient Stability of LiNiO₂ Lithium-Ion Battery Cathode Materials via Graphene-Cellulose Composite Coatings

Norman S. Luu, Patricia E. Meza, Andre M. Tayamen, Ozgenur Kahvecioglu, Sonal V. Rangnekar, Janan Hui, Julia R. Downing, and Mark C. Hersam*



Cite This: Chem. Mater. 2023, 35, 5150-5159



ACCESS I

III Metrics & More

Article Recommendations

s Supporting Information

ABSTRACT: Nickel-rich layered oxides are widely used as cathode materials for energy-dense lithium-ion batteries. These chemistries, based on the parent compound LiNiO_2 (LNO), are highly sensitive to ambient environments and are known to readily react with moisture and carbon dioxide. As a result, impurities such as lithium hydroxides and lithium carbonates are formed at the LNO surface, compromising electrochemical behavior. Here, we address this issue by coating LNO cathode particles with a hydrophobic barrier layer composed of graphene and ethyl cellulose (GrEC). This coating limits contact between atmospheric moisture and the LNO surface, which minimizes the generation of lithium impurities. This scheme is evaluated by exposing coated LNO to humidified CO_2 for 24 h as an accelerated ambient degradation test.



Subsequent spectroscopy, microscopy, and electrochemical characterization show no detectable signatures of carbonates on the LNO surface, thus verifying that the GrEC coating prevents ambient degradation. By demonstrating this methodology for the ultimate nickel-rich chemistry, this approach can likely be generalized to a wide range of ambient-sensitive battery materials.

INTRODUCTION

Lithium-ion batteries (LIBs) are playing a key role in the societal transition toward clean energy by serving as the technology of choice to power electric vehicles and grid-level energy storage.1 Current and emerging engineering applications demand battery packs with increasingly higher energy densities and longer lifetimes, necessitating intelligent materials selection of electrochemically active materials. For LIB cathode materials, Ni-rich layered oxide chemistries provide a pathway to address this need because they possess intrinsically high energy densities and lifetimes that can be tuned with careful control over transition metal content and operational states of charge.^{2,3} Incumbent Ni-rich LIB cathode materials include $LiNi_{0.8}Mn_{0.1}Co_{0.1}O_2$ (NMC811), $LiNi_{0.6}Mn_{0.2}Co_{0.2}O_2$ (NMC622), and LiNi_{0.8}Co_{0.15}Al_{0.05}O₂ (NCA), which are isostructural to the parent compound LiNiO₂ (LNO). The addition of dopant elements in these multicomponent lithium transition metal oxides (e.g., Mn, Co, and Al) helps increase cycling longevity. Nevertheless, these materials still show instabilities that can be traced back to the chemical reactivity of

Beyond cycling stability, recent work on Ni-rich LIB cathode materials has sought to understand and mitigate their high sensitivity to ambient conditions. Ni-rich layered oxides are known to readily react with atmospheric moisture and CO₂, forming LiOH on the oxide surface. The current understanding of this ambient degradation pathway involves two mechanisms, both requiring water as a reactant. One proposed

mechanism involves moisture-catalyzed transition metal reduction reactions, which are favorable due to the inherent reactivity of Ni^{3+} compared to Ni^{2+} . This pathway results in partial delithiation near the surface, with lithium sequestered in hydroxide deposits. A second proposed mechanism for the formation of LiOH involves H+-Li+ site exchange upon exposure to water, which has been well-documented as a consequence of washing Ni-rich layered oxides to remove undesirable lithium residues after synthesis. 9-11 After LiOH forms, it then readily reacts with ambient CO2, forming species such as LiHCO₃ or Li₂CO₃. Lithium bicarbonates can further react with LiOH to form H2O and Li2CO3 byproducts in an autocatalytic feedback loop. Following prolonged exposure to ambient conditions, where the supply of CO2 is effectively unlimited, lithium carbonate impurities are continuously generated until the available cathode surface area is depleted of reaction sites.

Surface hydroxides and carbonates are highly undesirable because they are detrimental to both electrochemical performance and cell manufacturing. Lithium impurities reduce firstcycle capacity due to their low electronic and ionic

Received: April 11, 2023 Revised: May 15, 2023 Published: June 22, 2023





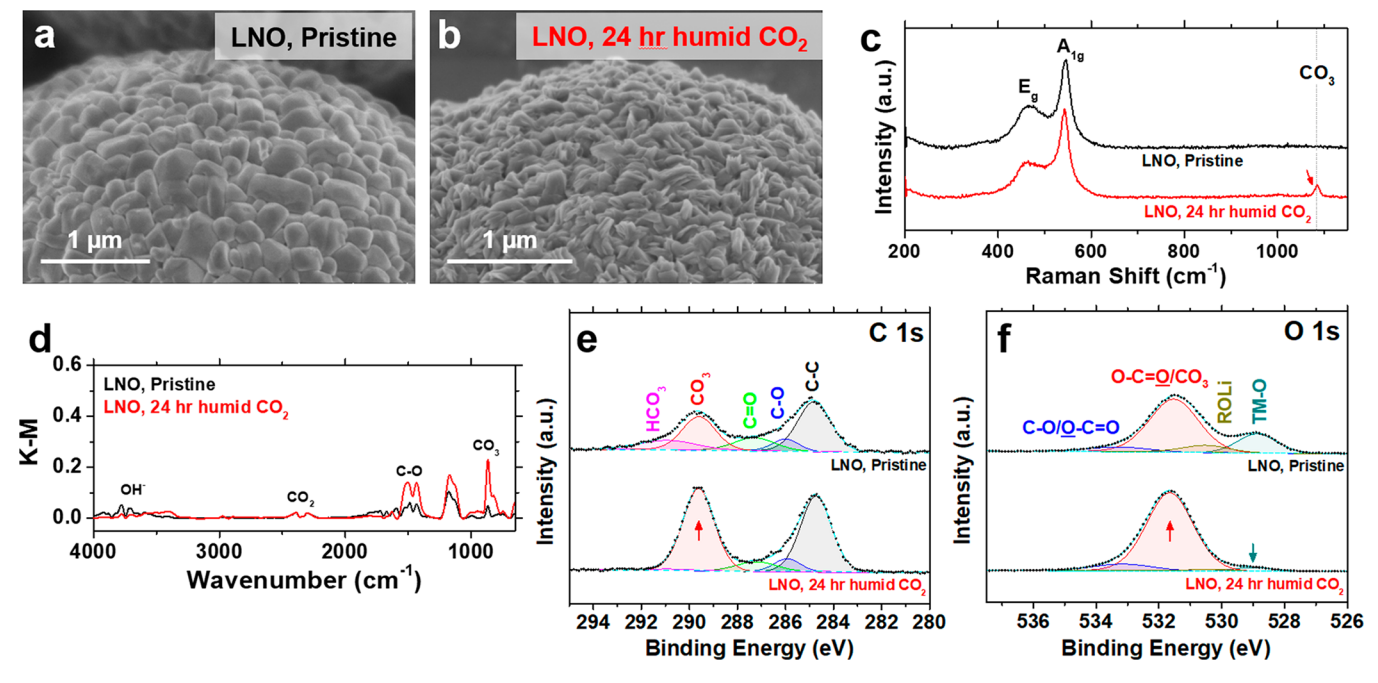


Figure 1. LNO exposed to humid CO₂ for 24 h exhibits severe morphological and surface chemical changes. (a, b) Scanning electron microscopy images of (a) pristine LNO and (b) LNO after being exposed to humid CO₂ for 24 h. (c) Raman, (d) DRIFTS-FTIR, (e) XPS C 1s, and (f) XPS O 1s spectra show the growth of surface carbonate species after exposure to humid CO₂.

conductivities, causing increased electrode polarization and charge transfer impedance. Furthermore, lithium carbonates on cathode surfaces promote electrolyte oxidation reactions and generate gas products during cycling, which compromise the long-term cycle life. At sufficiently high concentrations, surface hydroxides and carbonates are also known to cause slurry gelation, compromising electrode coating procedures that require strict control of slurry viscosity. Therefore, these surface species are typically removed from cathode powders prior to slurry mixing using methods such as acid treatments, 23–25 washing, 15,26 annealing, 7,18,27,28 and chemical conversion of lithium impurities. 25,29,30

A more attractive strategy is to inhibit the formation of surface hydroxides and carbonates altogether. Consequently, industrial facilities employ large dry rooms with tight limits on internal dew points for the storage and handling of Ni-rich LIB cathode powders. Because the operation of these dry rooms are expensive and energy-intensive, 31 strategies for preserving high-quality cathode surfaces in ambient conditions are of high interest to ease the demand for strict environmental control. One promising approach is to utilize hydrophobic coatings that prevent direct contact between ambient moisture and Ni-rich oxide surfaces. 32,33 Because the coating layer must also be electrochemically inert and transparent to lithium ions, compatible coating materials are highly limited and rarely employed in practice. To circumvent these restrictions, it would be ideal if LIB cathode surfaces could be protected with a barrier layer that could be removed on demand prior to electrochemical cycling.

In this work, we address the aforementioned issues of ambient-reactive Ni-rich layered oxides via a hydrophobic coating layer composed of graphene and ethyl cellulose (GrEC). We demonstrate this scheme for LNO because it represents the Ni-rich limit with the highest ambient sensitivity in the family of Ni-rich layered oxides. 4,34,35 Ethyl cellulose

(EC) is an attractive materials choice because it is hydrophobic 36–39 and can be scalably coated onto cathode material surfaces via solution-phase methods. EC can also be pyrolyzed thermally or photonically, enabling its removal immediately preceding electrochemical cycling. Notably, when this pyrolysis occurs in the presence of graphene, EC is known to decompose into low molecular weight aromatic carbon products, yielding carbonaceous residues with high sp² content that improves charge transport. ^{28,42–48} GrEC coatings therefore enable both long-term ambient storage and exceptional electrochemical performance for Ni-rich LIB cathode powders.

RESULTS AND DISCUSSION

LNO powders were synthesized via a hydroxide coprecipitation and calcination method, yielding secondary particles of LNO that were approximately 10 μ m in diameter (Figure S1). Scanning electron microscopy (SEM) showed that these secondary particles were composed of individual LNO grains, which each exhibited a smooth surface morphology (Figure 1a) immediately after particle synthesis. After 24 h of exposure to humidified CO2, the LNO surface became rough, with jagged features that rendered individual grains indistinguishable from one another (Figures 1b and S2). This transformation was indicative of degradation induced by the humid CO₂ exposure and was consistent with surface changes observed in other Ni-rich cathode systems. 26,27,32,49 To further investigate the chemical changes associated with this apparent surface morphological transformation, the degraded samples were interrogated with Raman spectroscopy, diffuse reflectance infrared Fourier transform spectroscopy (DRIFTS-FTIR), and X-ray photoelectron spectroscopy (XPS).

Raman spectroscopy of pristine LNO showed peaks that were assigned to the Ni–O A_{1g} (540 cm⁻¹) and the E_g (460 cm⁻¹) vibrational modes (Figure 1c, top), 4,14,50 with no other peaks clearly present. Surface-sensitive DRIFTS-FTIR of pristine LNO revealed spectral intensities at wavenumbers

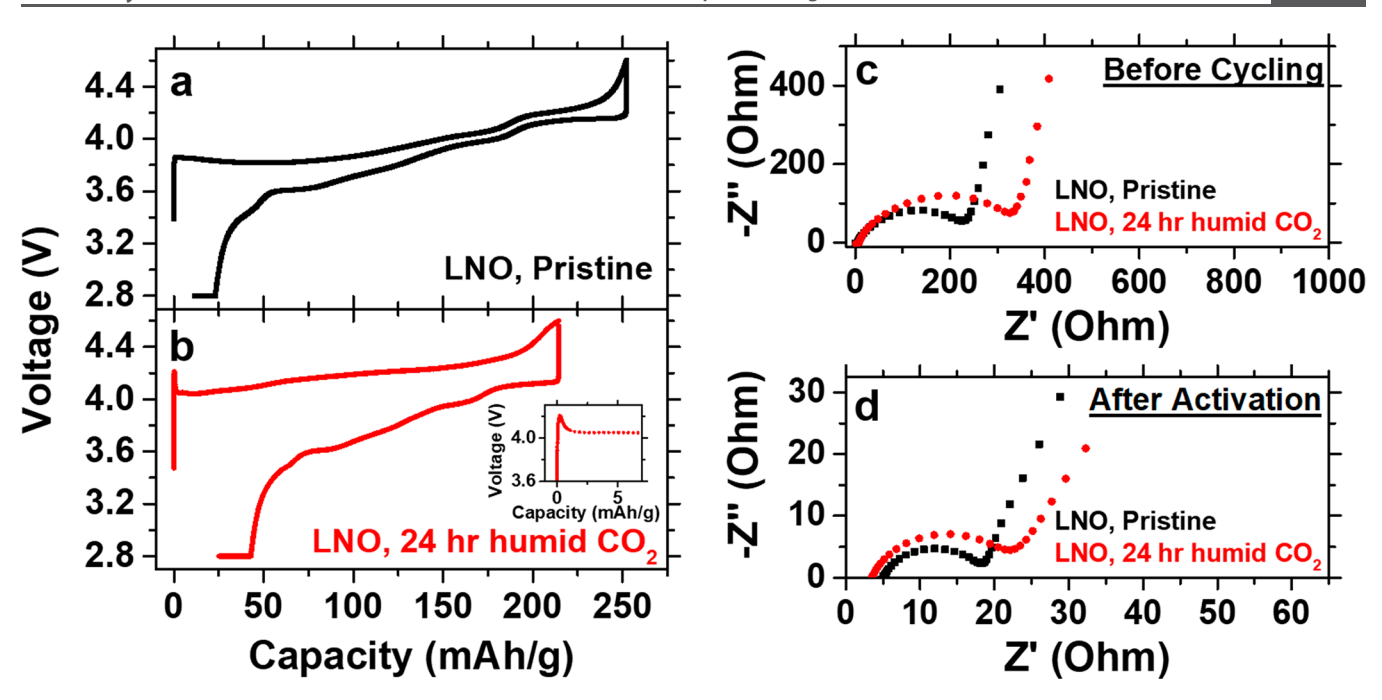


Figure 2. Electrochemical performance of uncoated LNO before and after humid CO_2 exposure. (a, b) Activation cycles of (a) pristine LNO and (b) LNO exposed to humid CO_2 . Activation was performed at C/10 with a constant voltage hold at 2.8 V vs Li/Li^+ until the current reached C/20. The inset in (b) shows a magnified view of the voltage peak present at the initial delithiation shoulder of LNO. (c, d) Nyquist plots (c) before cycling and (d) after activation for pristine LNO and LNO exposed to humid CO_2 .

consistent with C-O stretching (1500 and 1435 cm⁻¹) and CO₃ bending (865 cm⁻¹) (Figure 1d), which suggest that organic species and lithium carbonate impurities were weakly present. To further interrogate these surface species, XPS was used to carefully identify the chemical nature of the pristine LNO surface. The XPS C 1s spectrum was fit with component peaks assigned to adventitious C-C bonding at 284.8 eV, C-O bonding at 286 eV, and C=O bonding at 287.3 eV (Figure 1e, top). At higher binding energies, spectral intensities were observed and fit to lithium impurities CO₃ and HCO₃ at 289.6 and 290.9 eV, respectively. Meanwhile, the O 1s spectrum was fit with component peaks assigned to Ni-O bonding at 528.9 eV, ROLi bonding at 530.5 eV, O-C=Q/CO3 bonding at 531.5 eV, and C-O/O-C=O bonding at 533.2 eV (Figure 1f, top). Taken together, these results suggest that the pristine LNO was relatively clean, containing surface organic species and carbonate impurities that are generally expected for Nirich layered oxides following synthesis.¹⁸

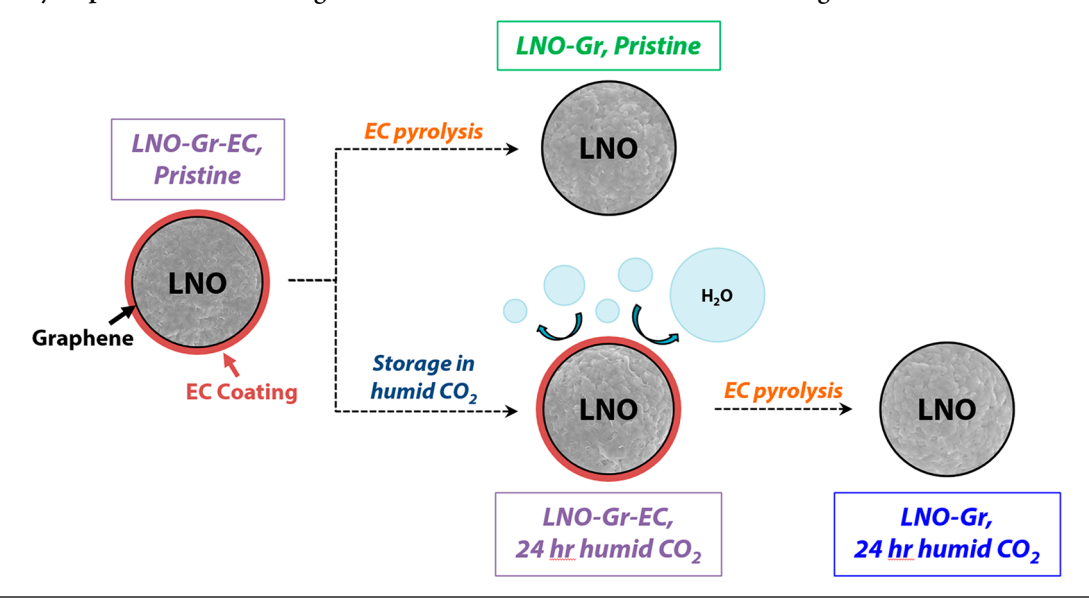
Exposure of the LNO to humid CO2 induced significant spectroscopic changes, which allowed chemical identification of the morphological changes observed in SEM. First, Raman spectroscopy (Figure 1c, bottom) showed the emergence of a peak at 1080 cm⁻¹ that was spectrally consistent with prior reports of carbonate vibrations in Ni-rich cathodes. 4,14,50 Second, DRIFTS-FTIR (Figure 1d) revealed that spectral intensities assigned to C-O stretching (1500 and 1430 cm⁻¹) and out-of-plane CO₃ bending (865 cm⁻¹) increased following exposure to humid CO₂, which is consistent with an increase in carbonate species on the LNO surface. 14,18,33,49-51 Finally, the XPS C 1s spectrum showed an increase in the carbonate spectral intensities after exposure to humid CO₂ (Figure 1e, bottom), while the XPS O 1s spectrum revealed that the carbonate spectral intensities increased simultaneously with decreased transition metal-oxygen (TM-O) bonding intensities (Figure 1f, bottom). Because these TM-O spectral

intensities originate from Ni–O bonding in LNO, these results suggest that an additional carbonate-rich layer is formed on the LNO surface during exposure to humid CO₂.

Humid CO₂ exposure severely degraded the electrochemical performance of uncoated LNO, which was evident in the initial activation cycle. As a baseline, pristine LNO achieved an initial charge capacity of 252 mAh g⁻¹ and a discharge capacity of 240 mAh g^{-1} , with low polarization during the charge discharge process (Figure 2a). In contrast, LNO exposed to humid CO₂ exhibited severe charge-discharge polarization, resulting in a low charge capacity of 214 mAh g⁻¹ and a corresponding discharge capacity of 189 mAh g⁻¹ (Figure 2b), which were ~15% and ~21% lower than the pristine LNO charge and discharge capacities, respectively. The shape of the initial charge process provided an additional signature of the carbonate impurities that were generated during humid CO₂ exposure. The initial delithiation voltage for LNO is known to occur at approximately 3.7 V vs Li/Li+, which was observed for pristine LNO. However, the voltage shoulder for LNO exposed to humid CO₂ was measured at approximately 4.0 V vs Li/Li⁺, corresponding to an ~300 mV overpotential. Moreover, above this voltage shoulder, a peak was evident (Figure 2b, inset), which has been observed previously and is characteristic of the electrochemical removal of impurity species on the LNO surface. 4,27,51 This feature was not present in the voltage profile for pristine LNO.

The increase in electrode polarization was also assessed via electrochemical impedance spectroscopy (EIS) and equivalent circuit modeling using a Randles circuit (Figures 2c,d and S3). Before activation, the charge transfer resistance was higher for the cell fabricated with LNO exposed to humid CO_2 (313.2 Ω) compared to pristine LNO (213.8 Ω). These results indicated that the surface layer of impurities that formed during humid CO_2 exposure was detrimental to the initial electrochemical behavior and further corroborated the observed polarization

Scheme 1. A Hydrophobic GrEC Coating Protects the LNO Surface from Ambient Degradation



increase in the voltage–capacity plots of the initial cycle. After activation, the cell fabricated with LNO exposed to humid CO_2 had a higher measured charge transfer resistance (17.2 Ω) compared to pristine LNO (12.1 Ω), suggesting that lithium impurities negatively impact cell behavior beyond the initial activation protocol.

To address the issue of ambient-induced degradation, LNO particles were encapsulated with a protective barrier layer to preserve the pristine surface state. Because the ambient degradation of Ni-rich layered oxides requires the presence of both moisture and CO₂ 7,18 limiting the availability of moisture via an external, the hydrophobic barrier layer is a promising strategy for preventing the formation of surface carbonates and hydroxides. 32,33 Toward this end, LNO particles were encapsulated with a GrEC coating (Scheme 1). Graphene and ethyl cellulose (EC) were selected due to their inherent hydrophobic character^{36–39} and combined ability to form a conformal coating on particles. In particular, the EC filled in gaps between the graphene nanoflakes, ensuring that the LNO particles were uniformly encapsulated and protected from ambient degradation. Because EC is electrically insulating, it is removed via a low-temperature pyrolysis step prior to electrochemical testing, which decomposes the EC into low molecular weight aromatic carbon with high sp² character.⁴² These carbonaceous residues bridge the graphene flakes, thus creating a percolating electronically conductive network throughout the electrode that aided charge transport as has been previously demonstrated for other Ni-rich cathodes such as NMC532,45 NCA,^{28,46} and LNO.⁴⁷

Experimentally, LNO particles were coated by homogeneously combining a GrEC dispersion in N-methyl-2-pyrrolidone (NMP) with LNO powder using a centrifugal mixer. A subsequent solvent removal step yielded LNO-Gr-EC, where the graphene and EC formed a uniform coating on the LNO surface (Figure 3a). The LNO-Gr-EC was then subjected to 24 h of exposure to humid $\rm CO_2$ and examined for changes to the particle surface morphology. SEM showed that the GrEC coating successfully preserved the quality of the LNO surface during the humid $\rm CO_2$ exposure, as evidenced by the lack of changes to the secondary particle shape (Figure 3b).

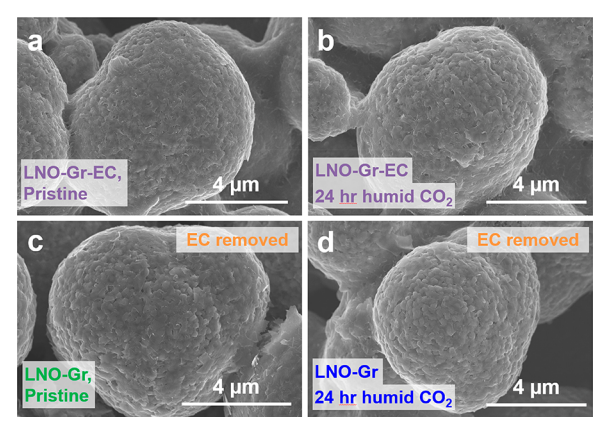


Figure 3. Scanning electron microscopy images show no changes in the surface morphology of the GrEC-coated LNO after 24 h of exposure to humid CO_2 . (a) As-coated LNO-Gr-EC, (b) coated LNO-Gr-EC after 24 h of exposure to humid CO_2 , (c) LNO-Gr obtained by pyrolyzing LNO-Gr-EC, and (d) LNO-Gr obtained by pyrolyzing LNO-Gr-EC after 24 h of exposure to humid CO_2 .

Individual primary particles of LNO were visible below the thin coating layer and exhibited no discernible changes in surface morphology, in contrast to the uncoated LNO exposed to humid $\rm CO_2$ (Figure 1b). Because any exposed LNO surfaces would rapidly react and form impurity species under these humid $\rm CO_2$ exposure conditions, the SEM images suggested that the GrEC coating was conformal and free of pinhole defects.

In preparation for electrochemical cycling and spectroscopic analysis, the EC layer was removed from the system by heating the LNO-Gr-EC in flowing O₂ to 300 °C, yielding LNO-Gr. The EC pyrolysis was conducted on as-coated samples (LNO-Gr, Figures 3c and S4) as well as samples that were coated and then exposed to humid CO₂ for 24 h (LNO-Gr, 24 h humid CO₂, Figures 3c and S5). Raman spectroscopy indicated that the graphene D/G ratio decreased after this heating step, confirming the decomposition of EC (Figure S6). The coating uniformity and quality were invariant even after thermal pyrolysis of EC, demonstrating that this scheme was

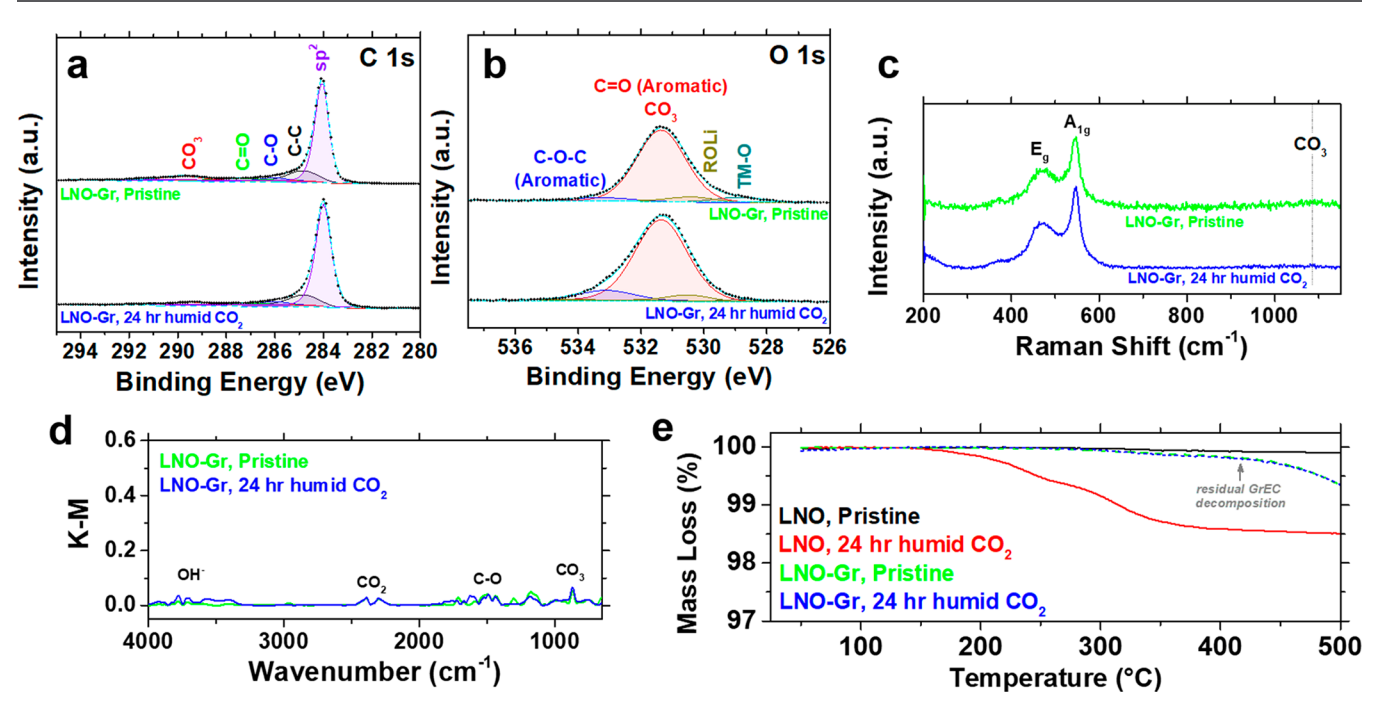


Figure 4. LNO-Gr shows minimal evidence of degradation after 24 h of exposure to humid CO_2 . (a) XPS C 1s spectrum, (b) XPS O 1s spectrum, (c) Raman spectroscopy, (d) DRIFTS-FTIR, and (e) thermogravimetric analysis show that the surface impurity species on LNO-Gr do not significantly increase despite 24 h of exposure to humid CO_2 .

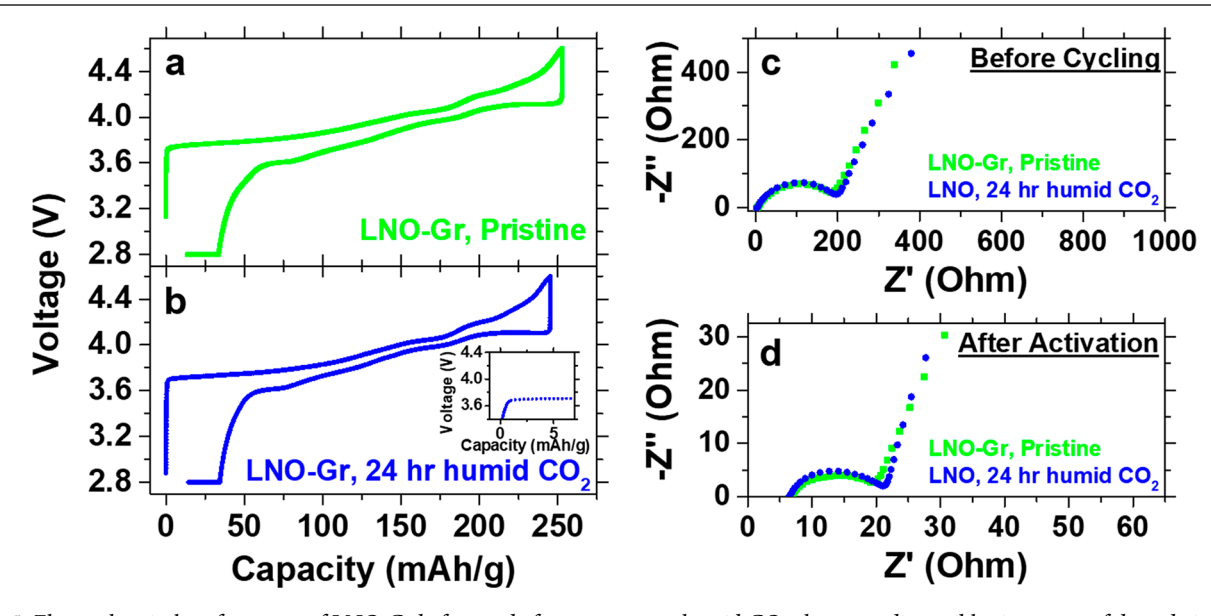


Figure 5. Electrochemical performance of LNO-Gr before and after exposure to humid CO_2 shows no discernible signatures of degradation. (a, b) Activation cycles of (a) pristine LNO-Gr and (b) LNO-Gr exposed to humid CO_2 . Activation was performed at C/10 with a constant voltage hold at 2.8 V vs Li/Li⁺ until the current reached C/20. The inset in (b) shows a magnified view of the initial delithiation shoulder of LNO-Gr without any voltage spike present. (c, d) Nyquist plots (c) before cycling and (d) after activation for pristine LNO-Gr and LNO-Gr exposed to humid CO_2 .

robust and yielded active materials that were compatible with subsequent electrode fabrication procedures.

Because the pyrolysis temperature of $EC^{28,45}$ (300 °C) is lower than the decomposition temperatures of LiHCO₃ (350 °C), LiOH (400 °C), or Li₂CO₃ (725 °C),^{7,18,27,50} surface impurities generated during exposure to humid CO₂ should be preserved following the EC removal step and thus detectable via subsequent spectroscopic analysis. To confirm whether the EC pyrolysis conditions were sufficient to induce changes in the surface morphology or chemistry, uncoated LNO that was exposed to humid CO₂ was subjected to the same thermal

treatment. Subsequent SEM, Raman, and XPS analysis of this powder showed that the rough surface morphology and carbonate spectral intensities persisted through the heating procedure (Figures S7–S9). These results suggest that if lithium impurities formed on the LNO-Gr-EC during storage, the EC removal step would not remove them from the LNO surface.

Following the removal of the EC coating, spectroscopic and gravimetric methods that directly interrogated the LNO-Gr surface revealed that the GrEC coating indeed mitigated the formation of surface carbonates and hydroxides upon the

exposure to humid CO₂. The XPS C 1s spectra were fit with the same component peaks as the uncoated LNO, with the addition of sp² bonding at 284.0 eV due to the presence of graphene. No significant changes were observed in the XPS C 1s spectra between the pristine and humid-CO2 LNO-Gr samples (Figure 4a). In the O 1s spectra, component peaks corresponding to aromatic $C=O/CO_3$ and C-O-C were assigned at 533.2 and 531.5 eV to account for the carbonaceous residue produced by EC pyrolysis (Figure 4b), but again no significant changes were observed between the pristine and humid-CO2 LNO-Gr samples. Similarly, the Raman spectra of the LNO-Gr samples before and after humid CO₂ exposure showed no appreciable differences, especially near the spectral vicinity of carbonate vibrational modes (1080 cm⁻¹, Figure 4c). This trend was also observed for the DRIFTS-FTIR spectra, which showed no substantial differences in the intensities corresponding to C-O stretching (1500 and 1435 cm⁻¹) and CO₃ bending (865 cm⁻¹, Figure 4d). Finally, because impurity species should desorb or decompose at high temperatures, thermogravimetric analysis (TGA) was performed to quantify the amount of impurity species present on the LNO (Figure 4e). Upon heating to 500 °C, the pristine LNO showed minimal mass loss (less than 0.1 wt %), suggesting that the LNO was relatively impurity-free. In contrast, the uncoated LNO exposed to 24 h of humid CO₂ lost 1.5% of its mass upon heating to 500 °C, which was attributed to the decomposition of carbonate species near 350 °C.^{7,2}

Compared to the uncoated LNO, the mass loss behavior for the GrEC-coated LNO before and after exposure to humid CO₂ was nearly identical (0.7 wt % loss at 500 °C), which suggested that the impurity levels on both samples were comparably low. Notably, both LNO-Gr samples exhibited a mass decrease beginning at approximately 300 °C. Because other analytical techniques suggested that the LNO-Gr sample was largely free of impurities, this mass loss was attributed to the pyrolysis of the carbonaceous residue that remained after the initial EC removal. To test this hypothesis, TGA was performed on GrEC powder that was prepyrolyzed under identical conditions as the LNO-Gr samples (Figure S10). The GrEC powder similarly showed mass loss below 500 °C, confirming that the mass loss observed for the LNO-Gr samples was due to the pyrolysis of residual carbon.

Finally, the LNO-Gr electrodes were galvanostatically cycled to search for electrochemical signatures of impurity species. During the activation cycle, the pristine LNO-Gr sample exhibited no evidence of compromised electrochemical behavior, achieving a charge capacity of 253 mAh g⁻¹ and a discharge capacity of 240 mAh g⁻¹ (Figure 5a). Similarly, the LNO-Gr sample after exposure to humid CO2 achieved a charge capacity of 245 mAh g⁻¹ and a discharge capacity of 230 mAh g⁻¹ without a discernible voltage peak at the shoulder near 3.7 V vs Li/Li⁺ (Figure 5b). The charge transfer resistances of the pristine LNO-Gr sample and the LNO-Gr sample after exposure to humid CO2 were similar before cycling (176.9 Ω vs 191 Ω , respectively; Figure 5c) and after activation (12.3 Ω vs 13.2 Ω , respectively; Figure 5d). To verify that the benefits of the GrEC coating extend beyond the first activation cycle, the LNO-Gr sample and the LNO-Gr sample after 24 h of exposure to humid CO2 were galvanostatically tested to 100 cycles. The extended cycling results showed nearly identical long-term cycling behavior for the two samples (Figure S11), thus confirming that the LNO

underneath the GrEC coating was essentially unchanged during humid CO_2 exposure. Altogether, the galvanostatic cycling and EIS results showed that the GrEC coating protected the LNO from degradation during exposure to humid CO_2 and had no deleterious effects on subsequent electrochemical behavior.

Overall, this work builds upon prior research that investigated the value imparted by GrEC coatings on a wide range of lithium-ion battery electrode chemistries in the context of cycling stability and electronic conductivity.^{28,43–47} This previous work extensively explored the beneficial impacts of GrEC coatings on LNO⁴⁷ and related layered oxides due to reduced chemomechanical degradation, suppressed deleterious phase transitions near the top of charge, and improved rate capability. 28,45,46 Building on this promising precedent, the research presented here further demonstrates that the same coating technology can address the ambient sensitivity of LNO, which has extremely strict storage requirements among the family of Ni-rich layered oxides. Therefore, this work establishes a secondary material platform that can be broadly applied not only to lithium-ion battery cathode materials but also to other ambient-reactive materials that can benefit from the additional electronic conductivity imparted by pyrolyzed GrEC coatings.

CONCLUSION

In this work, we addressed the ambient degradation of LNO by coating particles with a uniform, hydrophobic coating composed of graphene and ethyl cellulose. Compared to a control sample of bare LNO powder, which formed significant surface lithium impurities after 24 h of exposure to humid CO2, the coated LNO-Gr-EC was highly resistant to degradation. X-ray photoelectron, Raman, and DRIFTS-FTIR spectroscopies showed no spectral evidence of carbonate formation on LNO-Gr-EC after exposure to humid CO₂, corroborating the lack of surface morphological changes in SEM and mass changes in TGA. Moreover, the presence of lithium impurities is known to introduce greater electrode polarization, higher impedance, and a voltage peak near the delithiation shoulder in the activation cycle, indicating that the lithium impurities severely compromise electrochemical performance. These characteristics were clearly present for uncoated LNO following exposure to humid CO2 but were absent for the coated LNO-Gr-EC electrode exposed to the same conditions. Overall, this study establishes a scalable strategy for improving the ambient stability of Ni-rich cathode materials. By demonstrating this scheme for the Ni-rich limit of the layered lithium transition metal oxide family (i.e., LNO), this work can also be applied to related Ni-rich chemistries such as NMC and NCA that are widely used in electric vehicles and related energy storage technologies.

■ EXPERIMENTAL METHODS

LNO Synthesis. LNO powder was synthesized at the Argonne National Laboratory (ANL) Materials Engineering Research Facility (MERF) using a procedure that was slightly modified from previous reports. 52,53 In particular, Ni(OH) $_2$ precursor powders were synthesized continuously in a 10 L Taylor Vortex Reactor (TVR) via the hydroxide coprecipitation method using NiSO $_4\cdot 6H_2O$ as the starting material. Nickel sulfate salts were first dissolved in nitrogenpurged deionized water to obtain a 2 M solution. A 4 M solution of NaOH was employed as a coprecipitating agent, while the chelating agent was 4 M NH $_4OH$. The pH and temperature of the solution inside the reactor were maintained at 11.8 (± 0.02) and 50 °C (± 0.2

°C), respectively. The reactor was filled with nitrogen-purged deionized water before pumping in the reactants, and the inner cylinder was rotated at 900 rpm to create a Taylor vortex flow pattern inside the gap between two concentric cylinders where the reaction proceeded. The nickel sulfate solution was fed at ~17 mL min⁻¹, and NH₄OH was introduced at ~8.5 mL min⁻¹. The NaOH flow was adjusted to maintain the pH of the solution. The final precursor powder was produced continuously with a yield of $\sim 170 \text{ g h}^{-1}$. The precipitated product was washed thoroughly with nitrogen-purged deionized water until the conductivity of the solution was below 20 μ S cm⁻¹. The washed powder was then dried overnight at 120 °C under vacuum to obtain the hydroxide precursor with a tap density of 1.94 g cm⁻³ and particle size (D50) of 9.36 μ m. The final LNO powder was obtained after calcination with LiOH at 665 °C for 12 h with a heating ramp of 2 °C min⁻¹ under an O₂ atmosphere in a modified box furnace. The LNO powder had a final tap density of 2.31 g cm⁻³ and a particle size (D50) of 9.66 μ m. Prior to use, LNO powders were subjected to a low-temperature thermal cleaning process at 250 °C for 1 h under flowing oxygen to remove weakly adsorbed impurity species. The ramp rate used for this step was 5 °C min⁻¹. After cooling, the cleaned LNO powder was then immediately moved into an Ar glovebox (VAC Omni-Lab) with less than 0.5 ppm of oxygen for long-term storage.

Graphene-Ethyl Cellulose Production. Graphene-ethyl cellulose powder was produced using a previously established liquid-phase exfoliation method. ^{28,44–48} Briefly, 100 g of 150 mesh flake graphite (MilliporeSigma) was mixed with 6 g of ethyl cellulose powder (4 cP, MilliporeSigma) and 1 L of 200-proof ethanol in a Silverson L5M-A shear mixer at 10230 rpm for 2 h. The dispersion was retrieved and centrifuged for 20 min at 7500 rpm in a Beckman Coulter J26 XPI centrifuge to remove unexfoliated graphite, which was discarded. The supernatant from this step was then flocculated with a 0.04 g/mL solution of NaCl in water until the final dispersion reached a 1.74:1 ratio of graphene dispersion:sodium chloride solution. After a final centrifugation step at 7500 rpm for 7 min, the GrEC powder was harvested, rinsed with deionized water, vacuum filtered, and dried under infrared light overnight. The powder was analyzed using thermogravimetric analysis, which revealed that the GrEC powder was approximately 50 wt % graphene.

Humidity Exposure. A chamber was used to expose LNO powders to humid CO₂ (99.9% purity). Specifically, incoming CO₂ (99.9% purity) was humidified prior to reaching the chamber by flowing through an Erlenmeyer flask that was filled halfway with deionized water, placed on a hot plate set at 100 °C, and sealed with a rubber stopper. Two plastic tubes were inserted into the two holes in the rubber stopper to supply incoming dry CO₂ and carry outgoing humidified CO₂, allowing the flask to function as a bubbler. A small hygrometer was left inside the chamber to measure the internal relative humidity, which was approximately 60% RH during gas flow. After humidity exposure, the powder was retrieved and dried in an 80 °C vacuum oven (ThermoFisher Lindberg Blue M) overnight to desorb additional moisture prior to subsequent analysis and electrode fabrication. The powder was then moved into an Ar glovebox (VAC Omni-Lab) for long-term storage.

Electrode Fabrication. Control electrodes were fabricated by mixing a 90:5:5 mass ratio of LNO, Super P conductive carbon black (MTI Corporation), and poly(vinylidene fluoride) (PVDF, MTI Corporation). To improve slurry homogeneity, the PVDF was dissolved in N-methyl 2-pyrrolidone (NMP, anhydrous, MilliporeSigma) at 60 °C overnight to form a 6 wt % solution. The PVDF solution and carbon black were first mixed with additional NMP such that the total solids percentage in the final slurry was approximately 45 wt %. Mixing was performed in a centrifugal mixer (Thinky USA) at 800 rpm for 3 min, 1200 rpm for 3 min, 1600 rpm for 3 min, 2000 rpm for 3 min, and 2000 rpm for 3 min. In between each mixing step, the slurry was allowed to rest for 1 min without agitation. After a homogeneous slurry of carbon black, PVDF, and NMP was obtained, LNO was added and mixed again using the same protocol. The slurry was then cast onto carbon-coated aluminum foil (MTI Corporation), dried in a convection oven set at 120 °C for 15 min (BINDER GmbH), and followed by a final drying step under dynamic vacuum at 80 $^{\circ}$ C overnight (ThermoFisher Lindberg Blue M). The resulting active material loading was approximately 5 mg_{LNO} cm⁻². Electrode discs were punched out and calendered to a final electrode porosity of approximately 40% using an electric cold roller press (MTI Corporation).

To coat LNO particles, GrEC powder was first dispersed in a 5.33:1 vol/vol mixture of ethanol and NMP (anhydrous, MilliporeSigma). The ratio of ethanol to graphene in the mixture was approximately 5 mg mL⁻¹. To impart mechanical stability to the coating, multiwalled carbon nanotubes (MWCNTs, MilliporeSigma) were also added such that the mass ratio of graphene to MWCNTs was approximately 8:1. These components were homogeneously dispersed using a Fisher Scientific Sonic Dismembrator Model 500 equipped with a 1/4 in. tip for 1 h at a power output of 40 W. Next, the dispersion was placed on a hot plate set at 90 °C to evaporate the ethanol. LNO powder was added to the dispersion at a 97.5:2 mass ratio of LNO to graphene and homogeneously incorporated into the dispersion using a centrifugal mixer (Thinky USA). The mixing protocol used was 800 rpm for 3 min, 1200 rpm for 3 min, 1600 rpm for 3 min, 2000 rpm for 3 min, and 2000 rpm for 3 min, with a 1 min rest period in between each mixing step. The dispersion was used for electrode preparation by casting onto aluminum foil, drying at 120 °C for 15 min in a convection oven (BINDER GmbH) and a final step in an 80 °C vacuum oven (ThermoFisher Lindberg Blue M) for overnight drying. LNO-GrEC electrodes with active material loadings of approximately 5 mg_{LNO} cm⁻² were punched out and calendered identically to the control electrodes. Ethyl cellulose (EC) pyrolysis was accomplished by heating samples under flowing O2 in a tube furnace (ThermoFisher Lindberg Blue M) to 300 °C for 1 h at a 5 °C min⁻¹ ramp rate.

Coin cells (2032-type) were assembled in an Ar glovebox (VAC Omni-Lab). Cells were assembled with Celgard 2325 as the separator and lithium metal (China Energy Lithium, Co.) as the counter electrode. In each coin cell, 100 μ L of 1 M LiPF₆ in ethylene carbonate/ethyl methyl carbonate (EC/EMC, 50/50 v/v, MilliporeSigma) was used as the electrolyte.

Electrochemical Characterization. Galvanostatic cycling was performed between 2.8 and 4.6 V vs Li/Li⁺ with an Arbin LBT-20084 64-channel battery cycler. The cells were activated with five cycles at 0.1 C using a constant-current constant-voltage protocol on discharge, where the voltage was held constant at the end of the discharge step until a cutoff value of C/20. During extended cycling, the cells were charged and discharged at 1 C. Here, 1 C is defined as the current required to fully discharge LNO in 1 h. Electrochemical impedance spectroscopy (EIS) measurements were performed on fully discharged cells using a Bio-Logic VSP potentiostat between 1 MHz and 10 mHz. Equivalent circuit modeling was performed using the EC-Lab software (Biologic).

Scanning Electron Microscopy (SEM). A Hitachi SU8030 scanning electron microscope was used for SEM. Powder was deposited onto double-sided carbon tape adhered to an SEM stub. Prior to imaging, samples were also coated with 7 nm of Os using an osmium coater (SPI supplies). Imaging was performed at an accelerating voltage of 2 or 10 kV and a current of 10 mA.

X-ray Photoelectron Spectroscopy (XPS). XPS analysis was performed using a Thermo Scientific ESCALAB 250 Xi+ (Al $K\alpha$ radiation, ~1486.6 eV) at a base pressure of ~2 \times 10⁻⁸ Torr and an analysis spot size of 900 μ m. During the analysis, samples were charge compensated with a flood gun. Depth profiling was performed with an Ar⁺ gun at 2 keV, corresponding to an approximate etching rate of 0.11 nm s⁻¹. To prepare samples for analysis, a spatula was used to press powder onto double-sided copper adhesive tape on the sample holder, which left an optically dense layer of LNO. The amount of ambient exposure time during this step was less than 30 s. Peak fitting was performed using the Thermo Scientific Avantage software, with charge calibration set to adventitious carbon at ~284.8 eV.

Fourier Transform Infrared (FTIR) Spectroscopy. FTIR spectroscopy was performed in diffuse reflectance mode using a Nicolet iS50 spectrometer (Thermo Fisher) equipped with a DRIFTS

module. To prepare samples for DRIFTS-FTIR, KBr powder was mixed with LNO at a ratio of 99:1 using a mortar and pestle inside an Ar glovebox. Spectra were acquired with an average of 64 scans at a resolution of 4 cm $^{-1}$. Because the scans were conducted in ambient conditions with CO_2 present, the spectra of the LNO powders were normalized using the intensities of the CO_2 doublet (located at 2330 and 2360 cm $^{-1}$) to allow for direct comparison between samples.

Raman Spectroscopy. Raman spectroscopy was conducted using a HORIBA LabRAM HR Evolution Confocal Raman microscope equipped with a 532 nm laser. 60 spectra were acquired and averaged using a 600 g/mm grating for 5 s.

Thermogravimetric Analysis (TGA). Thermogravimetric analysis was performed using a Mettler Toledo TGA/DSC 3+ under flowing dry air. Prior to TGA, all powders were dried at 80 °C under dynamic vacuum to desorb moisture and then loaded into alumina crucibles for data acquisition.

ASSOCIATED CONTENT

Supporting Information

The Supporting Information is available free of charge at https://pubs.acs.org/doi/10.1021/acs.chemmater.3c00851.

SEM images; Raman spectra; XPS data; TGA data; equivalent circuit model (PDF)

AUTHOR INFORMATION

Corresponding Author

Mark C. Hersam — Department of Materials Science and Engineering, Northwestern University, Evanston, Illinois 60208, United States; Applied Physics Program, Department of Chemistry, and Department of Electrical and Computer Engineering, Northwestern University, Evanston, Illinois 60208, United States; Orcid.org/0000-0003-4120-1426; Email: m-hersam@northwestern.edu

Authors

- Norman S. Luu Department of Materials Science and Engineering, Northwestern University, Evanston, Illinois 60208, United States
- Patricia E. Meza Department of Materials Science and Engineering, Northwestern University, Evanston, Illinois 60208, United States
- Andre M. Tayamen Department of Materials Science and Engineering, Northwestern University, Evanston, Illinois 60208, United States
- Ozgenur Kahvecioglu Argonne National Laboratory, Lemont, Illinois 60439, United States
- Sonal V. Rangnekar Department of Materials Science and Engineering, Northwestern University, Evanston, Illinois 60208, United States
- Janan Hui Department of Chemistry, Northwestern University, Evanston, Illinois 60208, United States
- Julia R. Downing Department of Materials Science and Engineering, Northwestern University, Evanston, Illinois 60208, United States

Complete contact information is available at: https://pubs.acs.org/10.1021/acs.chemmater.3c00851

Notes

The authors declare the following competing financial interest(s): M.C.H. declares a financial interest in Volexion, Inc., which is a spinout company focused on high-performance LIB cathode materials.

ACKNOWLEDGMENTS

ACKNOWLEDGMENTS The authors thank Dr. Kyu-Young Park and Dr. Jin-Myoung Lim for early discussions on this project. This work was primarily supported by the National Science Foundation Future Manufacturing Research Program (NSF CMMI-2037026). This work made use of the Keck-II and EPIC facilities of the Northwestern University NUANCE Center, which has received support from the SHyNE Resource (NSF ECCS-1542205) and the Northwestern University MRSEC program (NSF DMR-1720139). This work also made use of the MatCI Facility supported by the Northwestern University MRSEC program (DMR-1720139. The cathode powder was produced at the Materials Engineering Research Facility (MERF) at Argonne National Laboratory. MERF is supported by the U.S. Department of Energy, Office of Energy Efficiency and Renewable Energy, and the Vehicle Technologies Office.

■ REFERENCES

- (1) Li, W.; Erickson, E. M.; Manthiram, A. High-Nickel Layered Oxide Cathodes for Lithium-Based Automotive Batteries. *Nature Energy* **2020**, 5 (1), 26–34.
- (2) Li, W.; Asl, H. Y.; Xie, Q.; Manthiram, A. Collapse of LiNi_{1-x-y}Co_xMn_yO₂ Lattice at Deep Charge Irrespective of Nickel Content in Lithium-Ion Batteries. *J. Am. Chem. Soc.* **2019**, *141* (13), 5097–5101.
- (3) Li, W.; Liu, X.; Xie, Q.; You, Y.; Chi, M.; Manthiram, A. Long-Term Cyclability of NCM-811 at High Voltages in Lithium-Ion Batteries: an In-Depth Diagnostic Study. *Chem. Mater.* **2020**, 32 (18), 7796–7804.
- (4) Jung, R.; Morasch, R.; Karayaylali, P.; Phillips, K.; Maglia, F.; Stinner, C.; Shao-Horn, Y.; Gasteiger, H. A. Effect of Ambient Storage on the Degradation of Ni-Rich Positive Electrode Materials (NMC811) for Li-Ion Batteries. *J. Electrochem. Soc.* **2018**, *165* (2), A132—A141.
- (5) Liu, H. S.; Zhang, Z. R.; Gong, Z. L.; Yang, Y. Origin of Deterioration for LiNiO₂ Cathode Material during Storage in Air. *Electrochem. Solid-State Lett.* **2004**, *7* (7), A190.
- (6) Shizuka, K.; Kiyohara, C.; Shima, K.; Takeda, Y. Effect of CO₂ on Layered Li_{1-x}Ni_{1-x-y}Co_xM_yO₂ (M = Al, Mn) Cathode Materials for Lithium Ion Batteries. *J. Power Sources* **2007**, *166* (1), 233–238.
- (7) Faenza, N. V.; Bruce, L.; Lebens-Higgins, Z. W.; Plitz, I.; Pereira, N.; Piper, L. F. J.; Amatucci, G. G. Growth of Ambient Induced Surface Impurity Species on Layered Positive Electrode Materials and Impact on Electrochemical Performance. *J. Electrochem. Soc.* **2017**, 164 (14), A3727–A3741.
- (8) Liu, H.; Yang, Y.; Zhang, J. Investigation and Improvement on the Storage Property of LiNi_{0.8}Co_{0.2}O₂ as a Cathode Material for Lithium-Ion Batteries. *J. Power Sources* **2006**, *162* (1), 644–650.
- (9) Toma, T.; Maezono, R.; Hongo, K. Electrochemical Properties and Crystal Structure of Li⁺/H⁺ Cation-Exchanged LiNiO₂. *ACS Appl. Energy Mater.* **2020**, 3 (4), 4078–4087.
- (10) Hartmann, L.; Pritzl, D.; Beyer, H.; Gasteiger, H. A. Evidence for Li⁺/H⁺ Exchange during Ambient Storage of Ni-Rich Cathode Active Materials. *J. Electrochem. Soc.* **2021**, *168* (7), 070507.
- (11) Pritzl, D.; Teufl, T.; Freiberg, A. T. S.; Strehle, B.; Sicklinger, J.; Sommer, H.; Hartmann, P.; Gasteiger, H. A. Washing of Nickel-Rich Cathode Materials for Lithium-Ion Batteries: Towards a Mechanistic Understanding. *J. Electrochem. Soc.* **2019**, *166* (16), A4056—A4066.
- (12) You, Y.; Celio, H.; Li, J.; Dolocan, A.; Manthiram, A. Modified High-Nickel Cathodes with Stable Surface Chemistry Against Ambient Air for Lithium-Ion Batteries. *Angew. Chem., Int. Ed.* **2018**, 57 (22), 6480–6485.
- (13) Visbal, H.; Fujiki, S.; Aihara, Y.; Watanabe, T.; Park, Y.; Doo, S. The Influence of the Carbonate Species on LiNi_{0.8}Co_{0.15}Al_{0.05}O₂ Surfaces for All-Solid-State Lithium Ion Battery Performance. *J. Power Sources* **2014**, *269*, 396–402.

- (14) Chen, Z.; Wang, J.; Huang, J.; Fu, T.; Sun, G.; Lai, S.; Zhou, R.; Li, K.; Zhao, J. The High-Temperature and High-Humidity Storage Behaviors and Electrochemical Degradation Mechanism of Li-Ni_{0.6}Co_{0.2}Mn_{0.2}O₂ Cathode Material for Lithium Ion Batteries. *J. Power Sources* **2017**, 363, 168–176.
- (15) Renfrew, S. E.; Kaufman, L. A.; McCloskey, B. D. Altering Surface Contaminants and Defects Influences the First-Cycle Outgassing and Irreversible Transformations of LiNi_{0.6}Mn_{0.2}Co_{0.2}O₂. ACS Appl. Mater. Interfaces **2019**, 11 (38), 34913–34921.
- (16) Renfrew, S. E.; McCloskey, B. D. Quantification of Surface Oxygen Depletion and Solid Carbonate Evolution on the First Cycle of LiNi_{0.6}Mn_{0.2}Co_{0.2}O₂ Electrodes. *ACS Appl. Energy Mater.* **2019**, 2 (5), 3762–3772.
- (17) Renfrew, S. E.; McCloskey, B. D. Residual Lithium Carbonate Predominantly Accounts for First Cycle CO₂ and CO Outgassing of Li-Stoichiometric and Li-Rich Layered Transition-Metal Oxides. *J. Am. Chem. Soc.* **2017**, *139* (49), 17853–17860.
- (18) Sicklinger, J.; Metzger, M.; Beyer, H.; Pritzl, D.; Gasteiger, H. A. Ambient Storage Derived Surface Contamination of NCM811 and NCM111: Performance Implications and Mitigation Strategies. *J. Electrochem. Soc.* **2019**, *166* (12), A2322–A2335.
- (19) Zhai, Y.; Yang, W.; Ning, D.; Yang, J.; Sun, L.; Schuck, G.; Schumacher, G.; Liu, X. Improving the Cycling and Air-Storage Stability of LiNi_{0.8}Co_{0.1}Mn_{0.1}O₂ through Integrated Surface/Interface/Doping Engineering. *J. Mater. Chem. A* **2020**, 8 (10), 5234–5245.
- (20) Seong, W. M.; Kim, Y.; Manthiram, A. Impact of Residual Lithium on the Adoption of High-Nickel Layered Oxide Cathodes for Lithium-Ion Batteries. *Chem. Mater.* **2020**, 32 (22), 9479–9489.
- (21) Seong, W. M.; Cho, K.-H.; Park, J.-W.; Park, H.; Eum, D.; Lee, M. H.; Kim, I.-s. S.; Lim, J.; Kang, K. Controlling Residual Lithium in High-Nickel (>90%) Lithium Layered Oxides for Cathodes in Lithium-Ion Batteries. *Angew. Chem., Int. Ed.* **2020**, *59* (42), 18662–18669.
- (22) Bi, Y.; Li, Q.; Yi, R.; Xiao, J. To Pave the Way for Large-Scale Electrode Processing of Moisture-Sensitive Ni-Rich Cathodes. *J. Electrochem. Soc.* **2022**, *169* (2), 020521.
- (23) Ramakrishnan, S.; Park, B.; Wu, J.; Yang, W.; McCloskey, B. D. Extended Interfacial Stability through Simple Acid Rinsing in a Li-Rich Oxide Cathode Material. *J. Am. Chem. Soc.* **2020**, *142* (18), 8522–8531.
- (24) Kim, H.; Lee, K.; Kim, S.; Kim, Y. Fluorination of Free Lithium Residues on the Surface of Lithium Nickel Cobalt Aluminum Oxide Cathode Materials for Lithium Ion Batteries. *Materials & Design* **2016**, *100*, 175–179.
- (25) Liu, M.; Jiang, Y.; Qin, Y.; Feng, Z.; Wang, D.; Guo, B. Enhanced Electrochemical Performance of Ni-Rich Cathodes by Neutralizing Residual Lithium with Acid Compounds. ACS Appl. Mater. Interfaces 2021, 13 (46), 55072–55079.
- (26) Zheng, X.; Li, X.; Wang, Z.; Guo, H.; Huang, Z.; Yan, G.; Wang, D. Investigation and Improvement on the Electrochemical Performance and Storage of LiNiO₂-Based Materials for Lithium Ion Battery. *Electrochim. Acta* **2016**, *191*, 832–840.
- (27) Lv, C.; Li, Z.; Ren, X.; Li, K.; Ma, J.; Duan, X. Revealing the Degradation Mechanism of Ni-Rich Cathode Materials After Ambient Storage and Related Regeneration Method. *J. Mater. Chem. A* **2021**, 9 (7), 3995–4006.
- (28) Lim, J.-M.; Luu, N. S.; Park, K.-Y.; Tan, M. T. Z.; Kim, S.; Downing, J. R.; He, K.; Dravid, V. P.; Hersam, M. C. Enhancing Nanostructured Nickel-Rich Lithium-Ion Battery Cathodes via Surface Stabilization. *Journal of Vacuum Science & Technology A* 2020, 38 (6), 063210.
- (29) Xie, Q.; Manthiram, A. Long-Life, Ultrahigh-Nickel Cathodes with Excellent Air Storage Stability for High-Energy Density Lithium-Based Batteries. *Chem. Mater.* **2020**, 32 (17), 7413–7424.
- (30) Kim, Y.; Park, H.; Dolocan, A.; Warner, J. H.; Manthiram, A. Wet-CO₂ Pretreatment Process for Reducing Residual Lithium in High-Nickel Layered Oxides for Lithium-Ion Batteries. *ACS Appl. Mater. Interfaces* **2021**, *13* (23), 27096–27105.

- (31) Yuan, C.; Deng, Y.; Li, T.; Yang, F. Manufacturing Energy Analysis of Lithium Ion Battery Pack for Electric Vehicles. *CIRP Annals* **2017**, *66* (1), 53.
- (32) Doo, S. W.; Lee, S.; Kim, H.; Choi, J. H.; Lee, K. T. Hydrophobic Ni-Rich Layered Oxides as Cathode Materials for Lithium-Ion Batteries. *ACS Appl. Energy Mater.* **2019**, 2 (9), 6246–6253
- (33) Gu, W.; Dong, Q.; Zheng, L.; Liu, Y.; Mao, Y.; Zhao, Y.; Duan, W.; Lin, H.; Shen, Y.; Chen, L. Ambient Air Stable Ni-Rich Layered Oxides Enabled by Hydrophobic Self-Assembled Monolayer. *ACS Appl. Mater. Interfaces* **2020**, *12* (1), 1937–1943.
- (34) Mayer, J. K.; Huttner, F.; Heck, C. A.; Steckermeier, D.; von Horstig, M.-W.; Kwade, A. Investigation of Moisture Content, Structural and Electrochemical Properties of Nickel-Rich NCM Based Cathodes Processed at Ambient Atmosphere. *J. Electrochem. Soc.* 2022, 169 (6), 060512.
- (35) Choi, J.; Dong, L.; Yu, C.-Y.; O'Meara, C.; Lee, E.; Kim, J.-H. Relationship of Chemical Composition and Moisture Sensitivity in LiNi_xMn_yCo_{1-x-y}O₂ for Lithium-Ion Batteries. *Journal of Electrochemical Energy Conversion and Storage* **2021**, DOI: 10.1115/1.4051208.
- (36) Lu, Y.; Yuan, W. Superhydrophobic/Superoleophilic and Reinforced Ethyl Cellulose Sponges for Oil/Water Separation: Synergistic Strategies of Cross-linking, Carbon Nanotube Composite, and Nanosilica Modification. ACS Appl. Mater. Interfaces 2017, 9 (34), 29167–29176.
- (37) Liu, Y.; Deng, L.; Zhang, C.; Chen, K.; Feng, F.; Zhang, H. Comparison of Ethyl Cellulose-Gelatin Composite Films Fabricated by Electrospinning Versus Solvent Casting. *J. Appl. Polym. Sci.* **2018**, 135 (46), 46824.
- (38) Liu, Y.; Li, Y.; Deng, L.; Zou, L.; Feng, F.; Zhang, H. Hydrophobic Ethylcellulose/Gelatin Nanofibers Containing Zinc Oxide Nanoparticles for Antimicrobial Packaging. *J. Agric. Food Chem.* **2018**, *66* (36), 9498–9506.
- (39) Secor, E. B.; Dos Santos, M. H.; Wallace, S. G.; Bradshaw, N. P.; Hersam, M. C. Tailoring the Porosity and Microstructure of Printed Graphene Electrodes via Polymer Phase Inversion. *J. Phys. Chem. C* 2018, 122 (25), 13745–13750.
- (40) Secor, E. B.; Lim, S.; Zhang, H.; Frisbie, C. D.; Francis, L. F.; Hersam, M. C. Gravure Printing of Graphene for Large-area Flexible Electronics. *Adv. Mater.* **2014**, *26* (26), 4533–4538.
- (41) Secor, E. B.; Ahn, B. Y.; Gao, T. Z.; Lewis, J. A.; Hersam, M. C. Rapid and Versatile Photonic Annealing of Graphene Inks for Flexible Printed Electronics. *Adv. Mater.* **2015**, *27* (42), 6683–6688.
- (42) de Moraes, A. C. M.; Obrzut, J.; Sangwan, V. K.; Downing, J. R.; Chaney, L. E.; Patel, D. K.; Elmquist, R. E.; Hersam, M. C. Elucidating Charge Transport Mechanisms in Cellulose-Stabilized Graphene Inks. J. Mater. Chem. C 2020, 8 (43), 15086–15091.
- (43) Chen, K.-S.; Xu, R.; Luu, N. S.; Secor, E. B.; Hamamoto, K.; Li, Q.; Kim, S.; Sangwan, V. K.; Balla, I.; Guiney, L. M.; et al. Comprehensive Enhancement of Nanostructured Lithium-Ion Battery Cathode Materials via Conformal Graphene Dispersion. *Nano Lett.* 2017, 17 (4), 2539–2546.
- (44) Lim, J.-M.; Kim, S.; Luu, N. S.; Downing, J. R.; Tan, M. T. Z.; Park, K.-Y.; Hechter, J. C.; Dravid, V. P.; He, K.; Hersam, M. C. High Volumetric Energy and Power Density $\text{Li}_2\text{TiSiO}_5$ Battery Anodes via Graphene Functionalization. *Matter* **2020**, *3* (2), 522–533.
- (45) Luu, N. S.; Lim, J.-M.; Torres-Castanedo, C. G.; Park, K.-Y.; Moazzen, E.; He, K.; Meza, P. E.; Li, W.; Downing, J. R.; Hu, X.; et al. Elucidating and Mitigating High-Voltage Interfacial Chemomechanical Degradation of Nickel-Rich Lithium-Ion Battery Cathodes via Conformal Graphene Coating. ACS Appl. Energy Mater. 2021, 4 (10), 11069–11079.
- (46) Park, K.-Y.; Lim, J.-M.; Luu, N. S.; Downing, J. R.; Wallace, S. G.; Chaney, L. E.; Yoo, H.; Hyun, W. J.; Kim, H.-U.; Hersam, M. C. Concurrently Approaching Volumetric and Specific Capacity Limits of Lithium Battery Cathodes via Conformal Pickering Emulsion Graphene Coatings. *Adv. Energy Mater.* 2020, 10 (25), 2001216.

Chemistry of Materials Article pubs.acs.org/cm

- (47) Park, K.-Y.; Zhu, Y.; Torres-Castanedo, C. G.; Jung, H. J.; Luu, N. S.; Kahvecioglu, O.; Yoo, Y.; Seo, J.-W. T.; Downing, J. R.; Lim, H.-D.; et al. Elucidating and Mitigating High-Voltage Degradation Cascades in Cobalt-Free LiNiO2 Lithium-Ion Battery Cathodes. Adv. Mater. 2022, 34 (3), 2106402.
- (48) Secor, E. B.; Prabhumirashi, P. L.; Puntambekar, K.; Geier, M. L.; Hersam, M. C. Inkjet Printing of High Conductivity, Flexible Graphene Patterns. J. Phys. Chem. Lett. 2013, 4 (8), 1347-1351.
- (49) Wang, C.; Shao, L.; Guo, X.; Xi, X.; Yang, L.; Huang, C.; Zhou, C.; Zhao, H.; Yin, D.; Wang, Z. Air-Induced Degradation and Electrochemical Regeneration for the Performance of Layered Ni-Rich Cathodes. ACS Appl. Mater. Interfaces 2019, 11 (47), 44036-44045.
- (50) Li, J.; Wang, X.; Kong, X.; Yang, H.; Zeng, J.; Zhao, J. Insight into the Kinetic Degradation of Stored Nickel-Rich Layered Cathode Materials for Lithium-Ion Batteries. ACS Sustainable Chem. Eng. 2021, 9 (31), 10547–10556.
- (51) Grenier, A.; Liu, H.; Wiaderek, K. M.; Lebens-Higgins, Z. W.; Borkiewicz, O. J.; Piper, L. F. J.; Chupas, P. J.; Chapman, K. W. Reaction Heterogeneity in $\text{LiNi}_{0.8}\text{Co}_{0.15}\text{Al}_{0.05}\text{O}_2$ Induced by Surface Layer. Chem. Mater. 2017, 29 (17), 7345-7352.
- (52) Aryal, S.; Durham, J. L.; Lipson, A. L.; Pupek, K. Z.; Kahvecioglu, O. Roles of Mn and Co in Ni-Rich Layered Oxide Cathodes Synthesized Utilizing a Taylor Vortex Reactor. Electrochim. Acta 2021, 391, 138929.
- (53) Rodrigues, M.-T. F.; Gim, J.; Tornheim, A.; Kahvecioglu, O.; Luo, M.; Prado, A. Y. R.; Trask, S. E.; Croy, J.; Abraham, D. P. Concealed Cathode Degradation in Lithium-Ion Cells with a Ni-Rich Oxide. J. Electrochem. Soc. 2022, 169 (4), 040539.

NOTE ADDED AFTER ASAP PUBLICATION

Due to a production error, this paper was published ASAP on June 22, 2023, with the wrong Supporting Information file. The corrected version was reposted on June 29, 2023.

□ Recommended by ACS

Li_{0.5}La_{0.5}TiO₃ as an Ionic Conducting Additive Enhancing the High-Voltage Performance of LiNi_{0.8}Mn_{0.1}Co_{0.1}O₂ Cathodes in **Lithium-Ion Batteries**

Tianyang Wang, Jung-Hyun Kim, et al. AUGUST 12, 2023 ACS APPLIED MATERIALS & INTERFACES

Cobalt-Free Layered LiNi_{0.8}Mn_{0.15}Al_{0.05}O₂/Graphene Aerogel **Composite Electrode for Next-Generation Li-Ion Batteries**

Deniz Kuruahmet, Hatem Akbulut, et al.

APRIL 17, 2023

ACS OMEGA

READ M

Revealing the Relationships between Washing/Recalcination **Processes and Structure Performance of Ni-Rich Layered Cathode Materials**

Yongen Gao, Shuandi Hou, et al.

NOVEMBER 23 2022

ACS APPLIED ENERGY MATERIALS

READ **C**

Mechanical Pulverization of Co-Free Nickel-Rich Cathodes for Improved High-Voltage Cycling of Lithium-Ion Batteries

Ryan Brow, Arumugam Manthiram, et al.

JUNE 08, 2022

ACS APPLIED ENERGY MATERIALS

READ 🗹

Get More Suggestions >